AALTO UNIVERSITY SCHOOL OF ENGINEERING
Department of Mechanical Engineering

Aalto University
School of Engineering

Adeyinka Abass

Branch Crack Behaviour in Bearing Steel under Rolling Contact Fatigue

Thesis submitted in partial fulfilment of the requirements for the degree of Master of Science in Technology

Riihimäki, Jan 09, 2017

Supervisor: Professor Heikki Remes

Instructor: Professor Hisao Matsunaga

Aalto University
School of Engineering

Aalto University, P.O. BOX 11000, 00076 AALTO
www.aalto.fi
Abstract of master's thesis

Author Adeyinka Abass		
Title of thesis Branch Crack Behaviour in Bearing Steel under Rolling Contact Fatigue		
Department Department of Mechanical Engineering		
Professorship Technical Mechanics	Code of professorship K3006	
Thesis supervisor Professor Heikki Remes		
Thesis advisor Professor Hisao Matsunaga		
Date 09.01.2017	Number of pages 48	Language English

In rolling contact fatigue, cracks grow by tensile (Mode I) or shear modes (Mode II and III) under the material surface due to the complicated tri-axial stress state. Flaking type failure, such as bearings and rails, is essentially due to the crack growth behaviour of these cracks. In order to evaluate the fatigue strength under rolling contact loading, it is important to understand the characteristics of such cracks under complicated stress state.

The aim of this thesis was to study mixed mode behaviour of fatigue cracks, under cyclic shear stress and static compressive stress. Both experimental and numerical methods are applied. Experimental work consisted of the fatigue testing of bearing steel (SAE52100) under compressive mean stress. The test results show that resistance to mode I crack propagation increases with increasing compressive mean stress. In addition, non-propagating cracks, which are hardly observed at stress ratio R of -1 in high strength steel, were observed at R = -5 and -10. In the numerical investigations, stress intensity factor of complicated branch cracks in a plate (2D) under combined cyclic shear stress and static compressive stress was determined by finite element method. This study reveal the interaction behavior between the mode I and II cracks.

The experimental and simulation results showed that there is a competitive behaviour between the Mode I and Mode II crack growth. The role of the compressive mean stress is to suppress the Mode I crack propagation. The magnitude of the compressive mean stress required to suppress Mode I crack growth depends on the Mode II crack length and applied cyclic shear stress. It was also observed that mode I crack lengths, if long enough, may reduce the K_{II} of the Mode II crack even by 63%.

The observation of non-propagating cracks for high compressive mean stress is one of novel finding of this study. However, the physical reason for this is not yet know. This is left future work. Furthermore, the numerical investigations can be extended to study more detail the influence of crack surface friction on crack growth mechanics.

Keywords fatigue, fracture mechanics, low stress ratio, bearing steel, FEM, stress intensity factor, mode I crack propagation

FORWARD

My sincere gratitude to Emeritus Professor Yukitaka Murakami (Kyushu University, Japan) for introducing me to the world of Theory of Elasticity and Metal Fatigue, your way of teaching and relationship with students inspired me to pursue a career in this field.

Special thanks to Professor Hisao Matsunaga (Kyushu University, Japan) for providing me with this interesting topic and also for accepting me to his laboratory to do experimental work for this thesis. I appreciate all the supports you gave to me throughout the process of this work. I will also use this section to appreciate your students and my-co-researchers, Kentaro Wada and Saburo Okasaki for their support with experimental work and thesis discussion. It was an honour to work with you.

A special thanks to my dear friend, Mari Åman for your moral support all along, you always believe that I can do it. Thank you also for correcting some of my poor grammars in this work.

I want to thank my teacher and thesis supervisor at Aalto University, Professor Heikki Remes for his support and guidance and for carefully checking the contents of this work.

I also want to thank my colleagues in Konecranes for their support. Most especially my supervisor, Mats Åkesson for supporting me before and during the thesis period. A special thanks to my mentor, Mikko Jutila for those useful hints regarding the simulation part of this work and also for always been there to help me grow in my career.

Finally, I want to thank my dear wife for those motivation she constantly gave to me to get this thesis done as quickly as possible.

Riihimäki, Jan 09, 2017

Adeyinka Abass

Table of Contents

NOMENCLATURE

Symbols

P	Equivalent dynamic bearing load
C	Basic dynamic loading
P	Exponent for bearing type
S	Probability of survival
V	Stress volume of bearing material
a_1	life adjustment factor for reliability
a_2	life adjustment factor for material
a_3	life adjustment factor for operating condition
L_{10}	Basic rating life
τ_0	Maximum orthogonal shear stress in the contact
A, c, h	Experimentally determined bearing material constants
$area$	Area of defect
R	Stress ratio
σ	Normal stress
τ	Shear stress
σ_{ij}	Component of stress tensor
σ_w	Fatigue limit of a plain specimen
ΔK	Stress intensity factor range
K	Stress intensity factor
∞	Infinity

Abbreviations

HV	Vickers hardness
ISO	International organization for standardization
RCF	Rolling contact fatigue
EDM	Electrical discharge method
SIF	Stress intensity factor
NPC	Non-propagating crack
FEM	Finite element method
BFM	Body force method
DDM	Distributed dislocation method

Subscripts

min	Minimum
max	Maximum
m	Mean value
a	Amplitude
th	Threshold
I, II, III	Mode of the crack

1 INTRODUCTION

1.1 Background of the study

Ball and roller bearings are commonly used in simple and complex machinery e.g. bicycles, turbines, car engines, transmissions etc. They are used to allow rotary motion and designed to bear significantly large loads. Figure 1 shows two common type of bearings, rolling bearing and ball bearings and their components. Fatigue is the predominant mode of failure in rolling element bearings [1]. It is a continuous goal for bearing engineers to always develop advanced bearings that provide higher efficiency, lower friction and more reliable even in applications under adverse operating conditions [2].

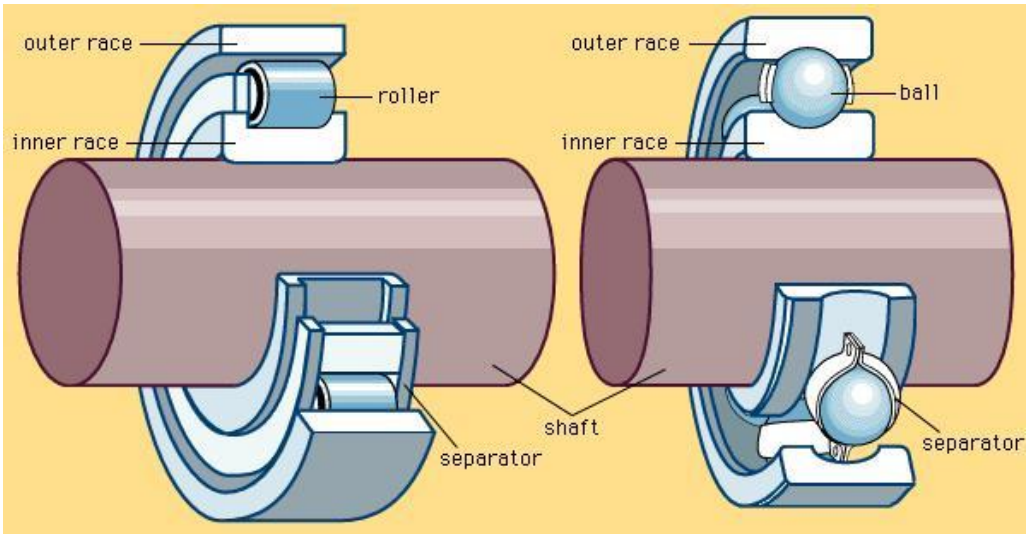

Figure 1 Rolling bearing (left) and ball bearing (right) [21]

Rolling Contact Fatigue (RCF) is the predominant mode of failure in rolling element bearings [1]. This phenomenon also occurs in other mechanical components involving rolling or sliding contacts such as gears, rail-wheel contacts and cam-follower mechanisms. RCF appears in many different mechanisms that ultimately result to final failure of the component [1, 2]. The two most dominant and widely researched RCF mechanisms are subsurface originating flaking and surface originated pitting. The dominant mechanics depends on a number of factors e.g., material quality, lubricant cleanliness, surface quality, etc.

Subsurface originated flaking occurs when micro-cracks originate below the surface at material inhomogeneities such as non-metallic inclusions and propagate toward the surface to form a surface flake, this process is often refer to as flaking. Factors which favours this mode of failure in RCF are smooth surfaces, presence of nonmetallic inclusions in the material, and absence of surface shear stresses. This mechanism is the dominant mode of failure in rolling element bearings that have good surface quality and is well lubricated [1-3]. Figure 2 is an example of the typical crack morphology due to subsurface originated flaking.

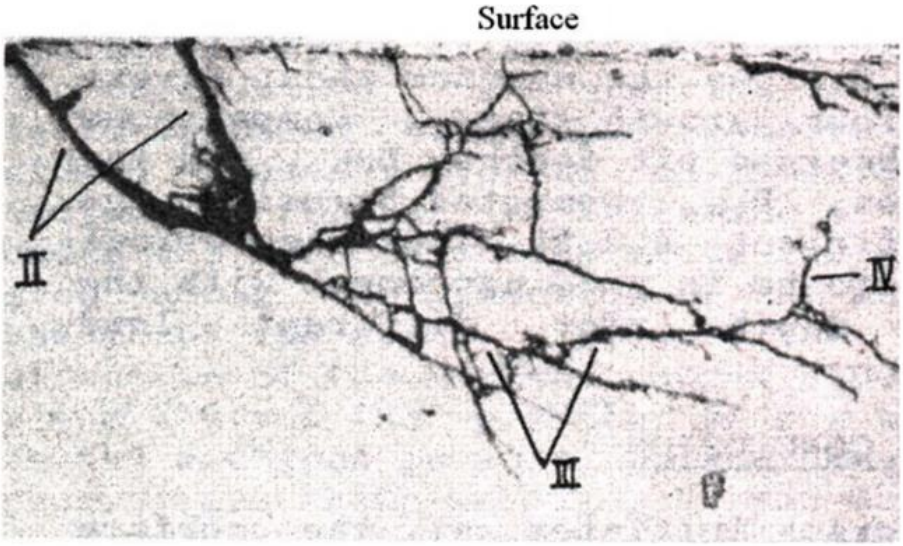

Figure 2 Subsurface cracks in rolling contact fatigue [3]

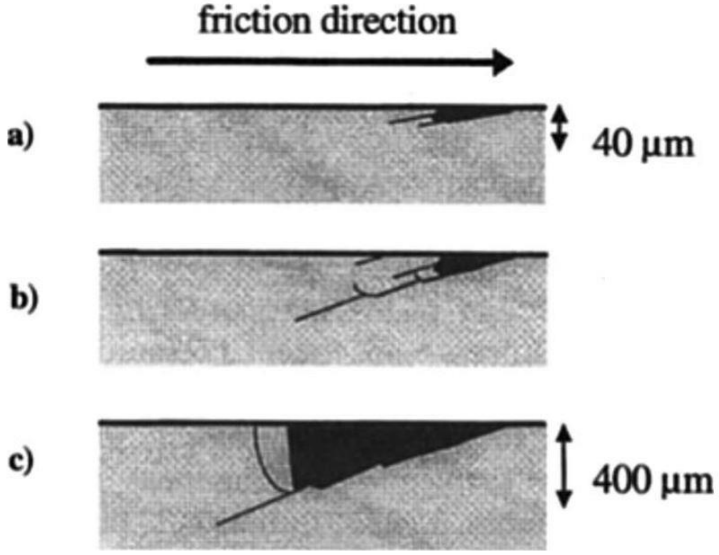

Figure 3 Mechanism of surface initiated pitting [3]

Surface originated pitting occurs in cases where surface irregularities in the form of dents or scratches are present. Cracks initiate at the surface stress concentrators and thereafter propagate at a shallow angle to the surface. When they reach a critical depth, the crack branch up toward the free surface, removing a piece of surface material and form a pit as shown in Figure 3 below [1-3].

It is well known that classical fatigue have some differences from RCF which makes results from classical fatigue not directly applicable to RCF. Sadeghi et al. [1] in his review of RCF made a compilation of the most important differences, they are listed as follows.

1. The state of stress in nonconformal contacts where RCF occurs is complex and multiaxial and governed by the Hertzian contact theory.
2. Contrary to most classical fatigue phenomena, rolling contact fatigue is typically multiaxial fatigue mechanism.
3. Contrary to classical fatigue, the loading history at a point below the surface is nonproportional; i.e., the stress components do not rise and fall with time in the same proportion to each other.
4. There is a high hydrostatic stress component present in the case of nonconformal contacts, which is absent in classical tension-compression or bending fatigue.
5. The principal axes in nonconformal contacts constantly change in direction during a stress cycle due to which the planes of maximum shear stress also keep changing. Thus, it is difficult to identify the planes where fatigue failure might initiate.
6. The phenomenon of RCF occurs in a very small volume of stressed material, because the contact stress field is highly localized.

Several investigators have proposed models to predict fatigue lives of bearing under RCF. A comprehensive discussion on this can be found in [1]. Sadeghi reported that between 1945 and 2007 over 30 models were proposed. This is an interesting figure because it shows the complex nature of the problem of RCF and also indicates that mechanism is not yet fully understood. Of these models, the Lundberg and Palmgren model is the most widely accepted model and will be discussed shortly.

The first theoretical basis for the formulation of a bearing life model was proposed by Lundberg and Palmgren [1-3]. They supposed that a crack initiates at subsurface due to the simultaneous occurrence at a particular depth of the maximum orthogonal shear stress and a weak point in the material. The hypothesized such weak points to be stochastically distributed in the material. The Weibull statistical strength theory was applied to the stressed volume in a pure Hertzian contact to obtain the probability of survival of the volume from subsurface initiated fatigue. The Lundberg-Palmgren theory states that for bearing rings subjected to N cycles of repeated loading the probability of survival S is given by

$$In\frac{1}{S} = A\frac{N^e \tau_0^c V}{z_0^h} \tag{1}$$

Where τ_0 the maximum orthogonal shear stress in the contact is, z_0 is the corresponding depth at which this stress occurs, and V is the stressed volume of the material. The parameters A, c and h are material characteristics that are determined experimentally. The parameter e is the Weibull slope for the experimental life data plotted on a Weibull probability paper. The stresses volume of material V was assumed to be

$$V = az_0\left(2\pi r_r\right) \tag{2}$$

where the dimensions a, z_0 and r_r correspond to the width, depth, and length of the volume as shown in Figure 4.

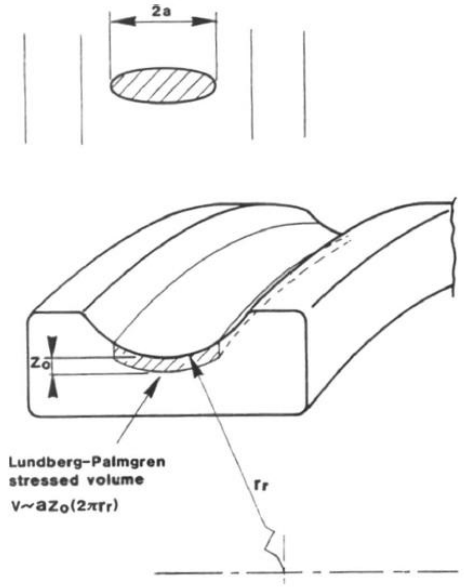

Figure 4 Stressed volume in the Lundberg-Palmgren theory [1]

The following load-life equation for the bearing was obtained by substituting for τ_0, z_0 and V in terms of the bearing dimensions and contact load in Equation 3,

$$L_{10} = \left(\frac{C}{P}\right)^p \tag{3}$$

Where, L_{10} is the life for 10% probability of failure, C is the bearing basic load rating, and P is the equivalent load on the bearing. The exponent P depends on bearing type.

The current ISO standard for rolling bearing life is based on a modification of the Lundberg-Palmgren equation and is given by

$$L = a_1 a_2 a_3 \left(\frac{C}{P}\right)^p \tag{4}$$

where a_1, a_2 and a_3 are life modifying factors that account for reliability, material, and operating conditions.

In classical fatigue, there exist a threshold stress amplitude such that the component is expected not to failure after a 10^6 or 10^7 cycles, such stress level is commonly refer to as endurance strength or fatigue limit. Prior to the discovery of the existence of the endurance strength for bearings by the FAG Kugelfischer research work in the 1970s, bearing life assessment was based on the L10DIN/ISO standards, otherwise known as the Lundberg and Palmgren model [2]. Figure 5 shows the correlation between the bearing life and the specific bearing stressing from FAG Kugelfischer test in comparison to the assumed life behaviour at that time. The result of their test demonstrated for the first time that endurance life can be achieved with rolling elements bearing. Despite this finding, L10DIN/ISO standard is still widely used till date.

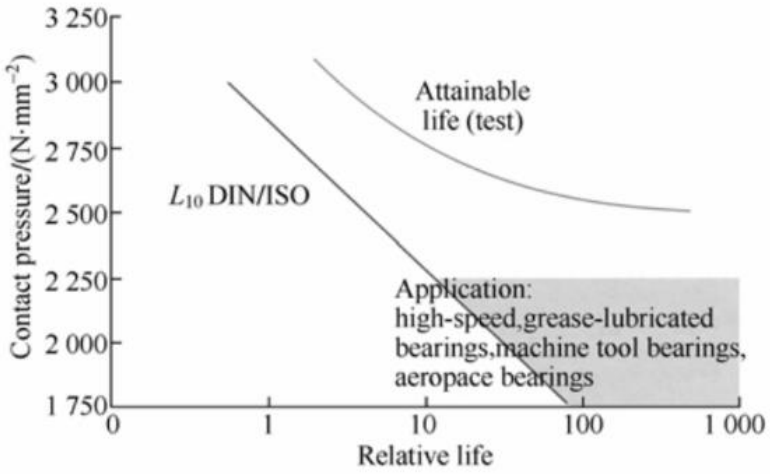

L_{10} DIN/ISO—Rated life with 10% failure probability

Figure 5 Actual attainable life in comparison to DIN/ ISO life calculation (unfactored) [2].

The bearing life and endurance strength are strongly dependent on the stress distribution, the conditions of lubrication, surface quality and cleanliness [3]. In order to design bearings with improved performance and fatigue life, it is important to understand how these factors affect the fatigue life of the rolling element.

The general method for determining the distribution of stresses in the zone of contact of two elastic bodies was first proposed by H. Hertz in 1881 [4]. Hertz derived mathematical expressions for the distribution of pressure on the contact area of bodies having an initial point contact. According to Hertz, the pressure distribution, shown in Figure 6, on the surface of two compressed bodies is defined by the expression

$$P = P_{\max}\sqrt{1-\frac{y^2}{b^2}} \tag{5}$$

where P_{max} = maximum pressure at centre of contact area

y = the distance from the x-axis

b = semi-axis of elliptical contact area

The value of P_{max} and b depends on the geometry and material of the two bodies in contact. For example, if two cylinders are in contacts, P_{max} and b is defined by the expressions

$$P_{\max} = \sqrt{\frac{1}{\pi\left(1-\nu^2\right)} \cdot \frac{P}{l} \cdot \frac{\frac{1}{R_1}+\frac{1}{R_2}}{\frac{1}{E_1}+\frac{1}{E_2}}} \tag{6}$$

$$b = 2\sqrt{\frac{1-\nu^2}{\pi} \frac{P\left(\frac{1}{E_1}+\frac{1}{E_2}\right)}{l\left(\frac{1}{R_1}+\frac{1}{R_2}\right)}} \tag{7}$$

where ν = Poisson's ratio for the two materials

P = force pressing the two cylinders together

E_1, E_2 = modulus of elasticity in compression for cylinders 1 and 2

R_1, R_2 = radii of the two cylinders

l = length of the cylinders

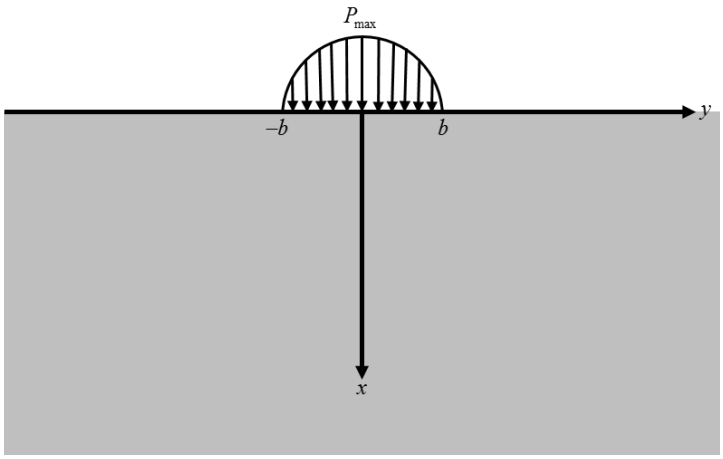

Figure 6 Pressure Distribution in Rolling Contact Loading.

In making this analysis, Hertz made the following assumptions:

1. The bodies in contact are isotropic
2. The proportional limit of materials is not exceeded

3. The loading acts perpendicular to the surface
4. The dimensions of the compressed area are small when compared with the whole surface of the bodies pressed together
5. The radii of curvature of the contact areas are very large compared with the dimensions of these area

Although Hertz completely solved this problem, the solution was left in term of certain Newtonian potential function [4]. The integral involved in this function was not expressed in terms of standard elliptic integrals. In 1924, Belayev [4] using the same assumptions found that the stresses on planes perpendicular to the coordinate axes can be calculated by the following equations:

$$\begin{aligned}
\sigma_{yy} &= -P_{\max} A_9 A_1 + P_{\max} A_1 A_2 \left(1 - \frac{A_7}{(A_8 - A_6)}\right) \\
\sigma_{xx} &= -P_{\max} A_9 A_1 - P_{\max} A_1 A_2 \left(1 - \frac{A_7}{(A_8 - A_6)}\right) \\
\sigma_{zz} &= -P_{\max} \frac{\lambda}{\lambda + \mu} A_9 A_1 \\
\tau_{xy} &= -P_{\max} A_2 A_1 \frac{A_5}{(A_8 - A_6)} \\
\tau_{yz} &= 0 \\
\tau_{xz} &= 0
\end{aligned} \tag{8}$$

Where,

$$A_1 = \sqrt{\frac{\left(b^2 - y^2 - x^2\right) + \sqrt{\left(b^2 - y^2 - x^2\right)^2 + 4b^2x^2}}{2b^2}}$$

$$A_2 = \sqrt{\frac{-\left(b^2 - y^2 - x^2\right) + \sqrt{\left(b^2 - y^2 - x^2\right)^2 + 4b^2x^2}}{2b^2}}$$

$$A_3 = \sqrt{1 - A_1^2}$$

$$A_4 = \sqrt{1 + A_2^2}$$

$$A_5 = 2A_1A_3$$

$$A_6 = 1 - 2A_1^2$$

$$A_7 = 2A_2A_4$$

$$A_8 = A_4^2 + A_2^2$$

$$A_9 = A_4 - A_2$$

λ and μ are Lame's constants and *b* is one-half of the contact strip.

It is revealing to study the distributions of the stress components σ_{xx}, σ_{yy}, σ_{zz} and τxy at some distance beneath the contact surface.

Consider the three lines L_1, L_2 and L_3 in Figure 7. The three lines are parallel to the contact surface and are located at position $x = 0.1b$, $0.5b$ and $1.0b$. The distribution of the stress components for lines L_1, L_2 and L_3 are shown in Figures 8, 9 and 10, respectively.

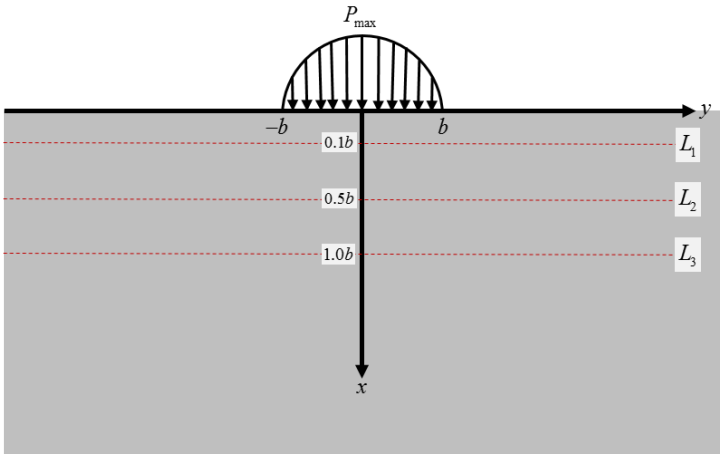

Figure7 Lines L_1, L_2 and L_3 beneath the contact surface.

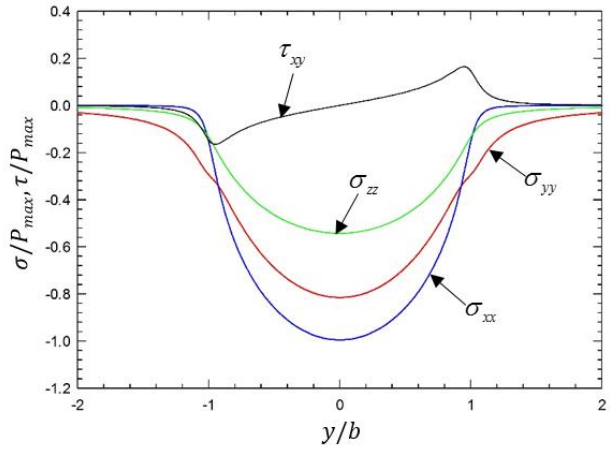

Figure 8 Variation of Stress Components in Contact Zone along x =0.1*b*.

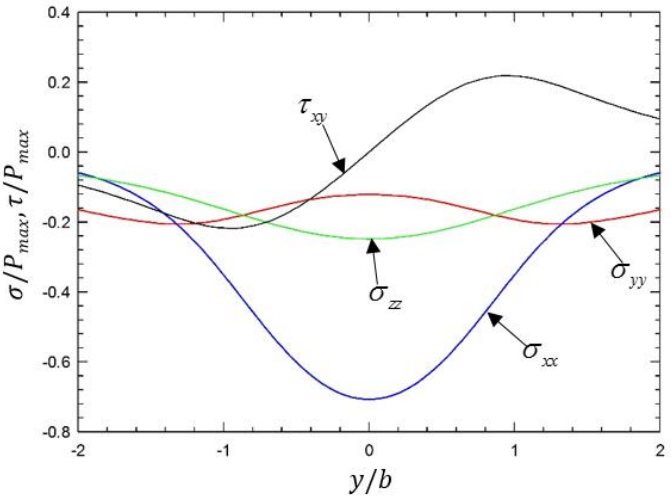

Figure 9 Variation of Stress Components in Contact Zone along x =0.5*b*.

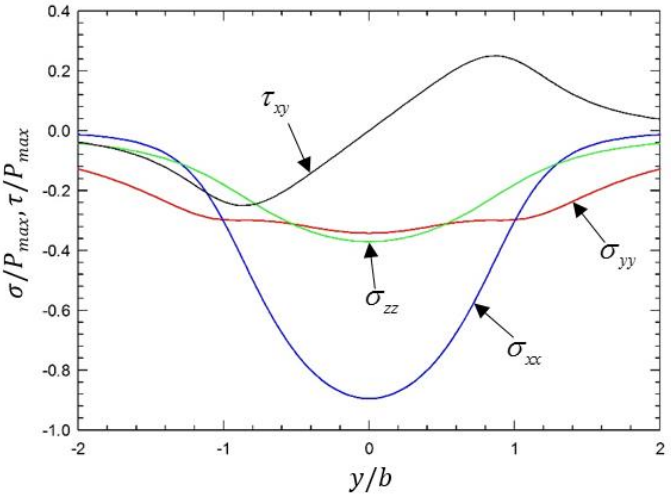

Figure 10 Variation of Stress Components in Contact Zone along x =1.0*b*.

Three important observations can be made from Figures 8, 9 and 10.

1. All normal stresses σ_{xx}, σ_{yy} and σ_{zz} are compressive stresses in the contact zone along lines L_1, L_2 and L_3.
2. The shear stress component, τ_{xy} is equal to zero at the plane of symmetry, increasing at first and then approaching zero asymptotically as the contact point moved away from the x-axis. τ_{xy} changes from $-\tau_{xy}$ to $+\tau_{xy}$ during the loading cycle.
3. The shear stress components, τ_{xy} reaches about its maximum value at $x = 0.5b$ from the contact surface (along line L_2). The maximum absolute value of the ordinates is located at about $y = \pm 0.85b$ from the line of symmetry and has a magnitude of $\left|\tau_{xy}^{\max}\right| \cong 0.25P_{\max}$.

From the point of view of fatigue failure, the second observations seem to point direction to τ_{xy} as the most essential stress component. The normal stresses σ_{xx}, σ_{yy} and σ_{zz} all varies from zero to negative maximum; therefore $\sigma_{min} = 0$ and the value of the Stress Ratio, R is always 0. The shear stress τ_{xy} ,on the other hand, varies from a positive maximum to a negative maximum value; hence the stress ratio, R is always -1. In addition to complex stress state, the effect of inclusions on the fatigue strength causes challenges. The effect of inclusions on fatigue strength of bearings has not be well understood and this has led to some wrong conclusions [5]. Murakami, in his work [5], pointed out that the size and shape of inclusions is the controlling factor of the fatigue life and strength in bearing steel, not the type of inclusion itself. This is contrary to the misconception in many literatures that "MnS is not detrimental when compared with other types of hard inclusions".

In conclusion, it can be said that a non-metallic inclusion (which can be essentially modelled as a small crack [5, 10]) beneath the contact surface experiences a fully reversed shear stress and (roughly speaking) high static compressive stress. A schematic of this loading is shown in Figure 11. Understanding this loading condition is crucial in planning experiments to study the mechanism of flaking of rolling element.

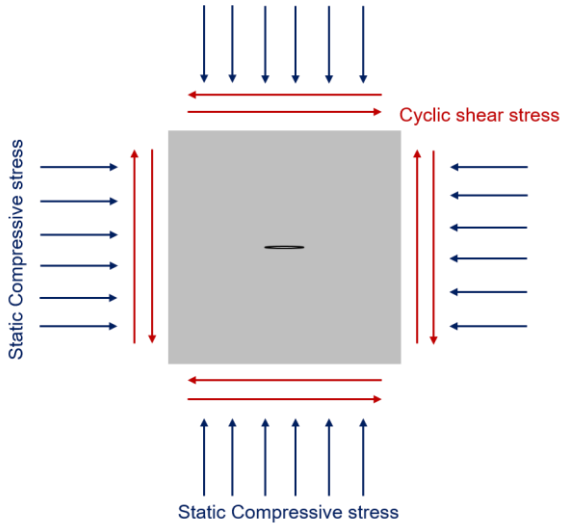

Figure 11 Loading Condition beneath the contact surface.

From the point of view of Linear Elastic Fracture Mechanics (LEFM), RCF can be interpreted by mixed mode fatigue crack growth. Based on LEFM three basic modes from the point of crack surface displacement view are Mode I (opening mode, crack surfaces move directly apart), Mode II (sliding mode, the crack surfaces move normal to the crack front and remain in the crack plane) and Mode III (tearing mode, the crack surfaces move parallel to the crack front and remain in the crack plane) as shown in Figure 12. The superimposition of these three modes is sufficient to describe the most general case of crack surface displacement.

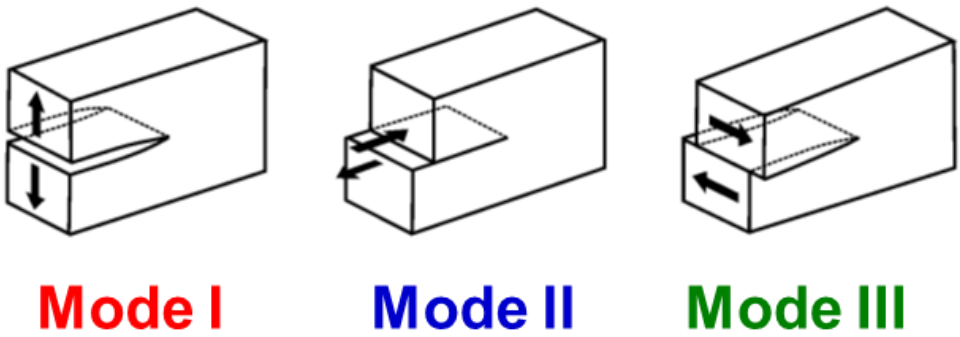

Figure 12 The three basic fracture modes.

Crack surfaces are stress stress-free boundaries adjacent to the crack tip and therefore dominate the distribution of stresses in that area. Remote boundaries and loading condition affect only the intensity of the stress field at the crack tip. These fields can be divided into three types corresponding to the three basic modes of crack surface displacement, and are generally characterized by the stress intensity factor K (with subscripts I, II, III to denote the mode). Let briefly examine the analytical solutions for the stress fields around the tip of a slit-like plane crack in an ideal Hookean continuum solid. This solution is often refer to as Irwin crack-tip solution.

Consider a slit in an infinite plate as shown in Figure 13. The singular crack tip stress fields, from which the corresponding displacement fields may be easily found by using Hooke's law and integrating, are given by the equations below [18].

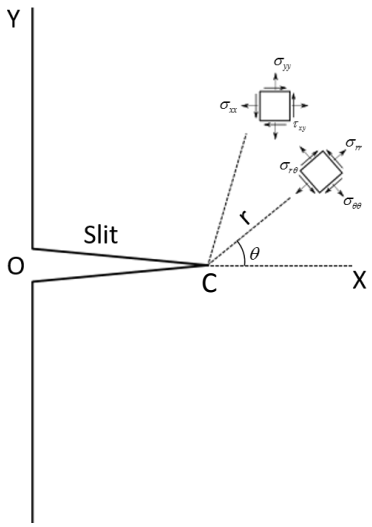

Figure 13 Stress field at Irwin slit-crack tip C, showing rectangular and polar-coordinate components.

The Irwin crack-tip solutions are given below for each of the three modes in relation to the coordinate system of Figure 13. The *K* terms are the stress-intensity factors, *v* is the Poisson's ratio, $\nu' = 0$ (plane stress) and $\nu' = \nu$ (plane strain).

Mode I:

$$\begin{Bmatrix}\sigma_{xx}\\ \sigma_{yy}\\ \tau_{xy}\end{Bmatrix}=\frac{K_I}{(2\pi r)^{1/2}}\begin{Bmatrix}\cos(\theta/2)\left[1-\sin(\theta/2)\sin(3\theta/2)\right]\\ \cos(\theta/2)\left[1+\sin(\theta/2)\sin(3\theta/2)\right]\\ \sin(\theta/2)\cos(\theta/2)\cos(3\theta/2)\end{Bmatrix}$$

$$\begin{Bmatrix}\sigma_{rr}\\ \sigma_{\theta\theta}\\ \tau_{r\theta}\end{Bmatrix}=\frac{K_I}{(2\pi r)^{1/2}}\begin{Bmatrix}\cos(\theta/2)\left[1+\sin^2(\theta/2)\right]\\ \cos^3(\theta/2)\\ \sin(\theta/2)\cos^2(\theta/2)\end{Bmatrix}$$

$$\sigma_{zz}=\nu'\left(\sigma_{xx}+\sigma_{yy}\right)=\nu'\left(\sigma_{rr}+\sigma_{\theta\theta}\right) \tag{9}$$

$$\tau_{xz}=\tau_{yz}=\tau_{rz}=\tau_{\theta z}=0$$

Mode II

$$\begin{Bmatrix}\sigma_{xx}\\ \sigma_{yy}\\ \tau_{xy}\end{Bmatrix}=\frac{K_{II}}{(2\pi r)^{1/2}}\begin{Bmatrix}-\sin(\theta/2)\left[2+\cos(\theta/2)\cos(3\theta/2)\right]\\ \sin(\theta/2)\cos(\theta/2)\cos(3\theta/2)\\ \cos(\theta/2)\left[1-\sin(\theta/2)\sin(3\theta/2)\right]\end{Bmatrix}$$

$$\begin{Bmatrix}\sigma_{rr}\\ \sigma_{\theta\theta}\\ \tau_{r\theta}\end{Bmatrix}=\frac{K_{II}}{(2\pi r)^{1/2}}\begin{Bmatrix}\sin(\theta/2)\left[1-3\sin^2(\theta/2)\right]\\ -3\sin(\theta/2)\cos^2(\theta/2)\\ \cos(\theta/2)\left[1-3\sin^2(\theta/2)\right]\end{Bmatrix}$$

$$\sigma_{zz}=\nu'\left(\sigma_{xx}+\sigma_{yy}\right)=\nu'\left(\sigma_{rr}+\sigma_{\theta\theta}\right) \tag{10}$$

$$\tau_{xz}=\tau_{yz}=\tau_{rz}=\tau_{\theta z}=0$$

Mode III

$$\sigma_{xx}=\sigma_{yy}=\sigma_{rr}=\sigma_{\theta\theta}=0$$

$$\tau_{xy}=\tau_{r\theta}=0$$

$$\begin{Bmatrix}\tau_{xz}\\ \tau_{yz}\end{Bmatrix}=\frac{K_{III}}{(2\pi r)^{1/2}}\begin{Bmatrix}-\sin(\theta/2)\\ \cos(\theta/2)\end{Bmatrix} \tag{11}$$

$$\begin{Bmatrix}\tau_{rz}\\ \tau_{\theta z}\end{Bmatrix}=\frac{K_{III}}{(2\pi r)^{1/2}}\begin{Bmatrix}\sin(\theta/2)\\ \cos(\theta/2)\end{Bmatrix}$$

The stress formulas in 9, 10, and 11 may be reduced to a particular simple and very informative form,

$$\sigma_{ij} = K\left(2\pi r\right)^{-1/2} f_{ij}\left(\theta\right) \tag{12}$$

If θ is taken as zero, equation (12) can be rewritten as,

$$K = \left(2\pi r\right)^{1/2} \sigma_{ij} \tag{13}$$

Equation 12 shows that Elastic stresses are inversely proportional to the square root of the distance from the crack tip, and become infinite at the crack tip. The representation of a crack tip stress field by a stress intensity factor is a basic concept in fracture mechanics.

In the analysis of fatigue crack growth data, the fatigue cycle is usually described by:

$$\Delta K = K_{\max} - K_{\min}\,, \tag{14}$$

where $K_{\max}$ and $K_{\min}$ are the maximum and minimum values of K during the fatigue cycle. ΔK is the stress intensity factor range. It has been shown experimentally that ΔK rather than $K_{\max}$ has the major influence on fatigue crack growth. If ΔK is below a certain threshold value ($\Delta K_{\mathrm{I,th}}$, $\Delta K_{\mathrm{II,th}}$ and $\Delta K_{\mathrm{III,th}}$), fatigue crack growth does not occur. Likewise, the behaviour and the material resistance to RCF can also be descripted by stress intensity factor range.

Nonmetallic inclusion in present day bearing steels are usually of small size, this is because the cleanliness of bearing steel has improved over the years [1, 2, 3, and 5]. Fatigue crack threshold ΔK_{th} for small cracks are not an intrinsic material property, but depend on the sizes of cracks, and decreases with decreasing crack size [5], hence it is important to clarify the small crack effect on both Mode-I and shear-mode crack growths. There has been several misconception in literature on what is a small/short crack. Most literature associate small crack behaviour with crack tip plasticity, however this is not true [5]. The crack size when it should be regarded as a small crack depends on the material and many other factors .In addition, it is important to understand the different between a short crack, a small crack, a long crack and a large crack. A short crack can be physically large and a long crack can be physically small from the point of view of its *area*. Detail discussion can be found in [5].

Murakami and Endo has provided experimental evidence [5] that from the point of view of fatigue limit, small defects, hole and nonmetallic inclusions can essentially be modelled as a small crack and he proposed the $\sqrt{area}$ as the geometric parameter relating the ΔK_{th} to the small crack size, irrespective of the material. The term " *area* " is the projection of the initial defect size to the principal plane. The relationship is given as:

$$\Delta K_{Ith} \propto \left(\sqrt{area}\right)^{\frac{1}{3}} \qquad \text{and} \qquad \Delta K_{\tau th} \propto \left(\sqrt{area}\right)^{\frac{1}{3}}$$

The effects of material hardness and mean stress on fatigue strength properties of materials containing small defects are different from those of long cracks or plain specimen as shown in Figure 14. In Figure 14(a), it can be seen that the fatigue limit σ_w of plain specimen has a positive linear dependency on material hardness. On the contrary, threshold stress intensity factor, ΔK_{th} of long crack shows a slightly negative dependency but small defect shows a positive dependency. The effect of mean stress on fatigue properties is shown in Figure 14(b), the thick line represent the fatigue limit prediction of modified Goodman equation, fatigue limit of plain specimen decreases as mean stress increases, the ΔK_{th} of long crack decreases and then level off at high mean stress. On the contrary, ΔK_{th} of small crack shows strong dependencies on material but this dependency level off at high tensile mean stress. It should be observed that the material dependency of mean stress effect becomes more pronounced as compressive mean stress increases. Experiment data of three different materials (S25C HV141,S45C HV261,SCM435 HV305) obtained by Kondo et.al shown in figure 15 is an evidence of this phenomenon. The concept of fatigue crack closure first introduced by Elber can be used to explain this phenomenon [11,12].

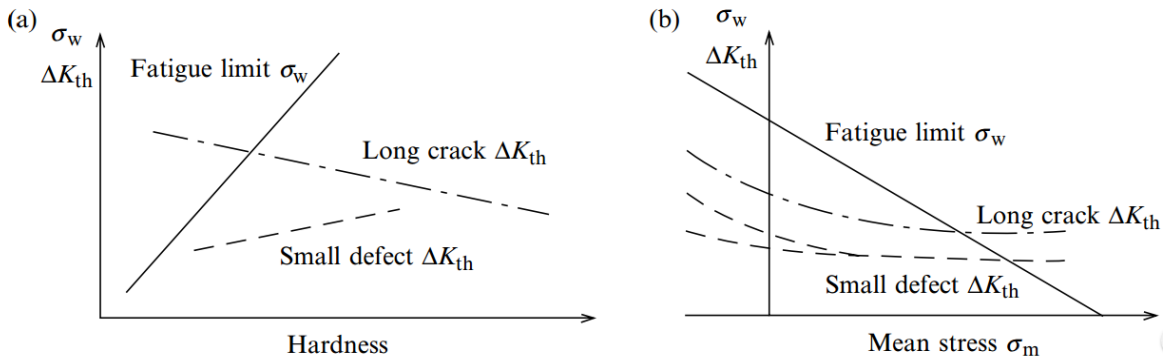

Figure 14 Effect of material hardness and mean stress on fatigue limit properties: (a) Effect of hardness, and (b) Effect of mean stress. [10]

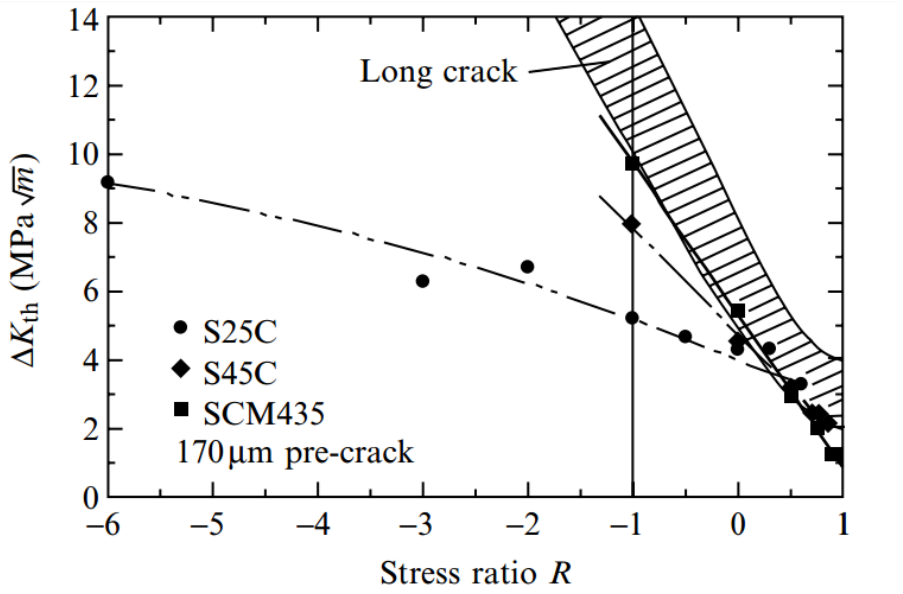

Figure15 ΔK_{th} of short cracks at the fatigue limit [10]

Fatigue failure of bearing steel with good surface condition under contact loading mostly initiates from subsurface non-metallic inclusion in the presence of high compressive stress in addition to the cyclic shear stress components [1, 3, 5, and 6]. For this reason, it is important to understand the influence of this high compressive stress on the fatigue crack initiation and propagation as well.

Subsurface originated fatigue failure is the most common type of failure in bearings having smooth surface and good lubrication [1]. Microcracks originate from non-metallic inclusions close to the surface of the rolling elements. This is also the region of maximum shear stress. Figure 2 (taken from [3]) shows the complex morphology of such cracks, which eventually lead to flaking.

A simplified model of the mechanism involved in subsurface flaking of bearing under RCF is shown in Figure 16. Figure 17 shows evidence of inclusion at the fracture origin of a bearing steel.

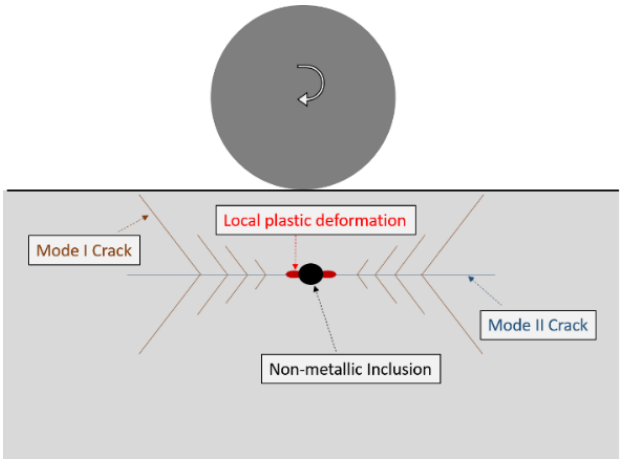

Figure 16 Mechanism of subsurface cracking in rolling contact fatigue.

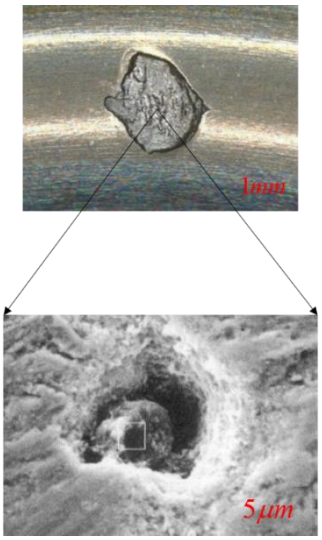

Figure 17 Non-metallic inclusion at fracture origin.

Mode I crack growth data and thresholds are relatively easy to obtain but Mode II and III crack growth data and thresholds are not so easily determined. This is because shear mode loading does not necessarily result to shear mode crack growth. Matsunaga et al. [8] in an attempt to obtain a stable shear-mode crack growth in SAE52100 bearing steel superposed static compressive stress on cyclic shear stress on a cylindrical specimen containing initial

artificial defects smaller than 1mm. The specimen and artificial defect used by Matsunaga [8] is shown in Figure 18.

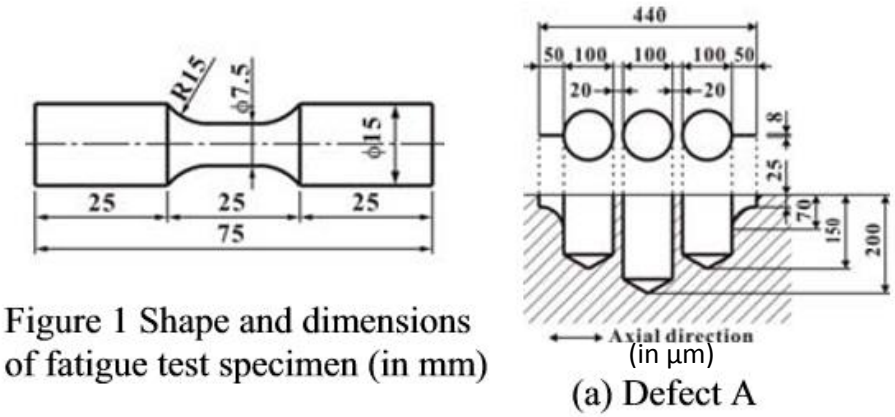

Figure 18 Shape and dimensions of test specimen and initial defect [8]

Figure 19 shows a crack propagating from the defect A at τ_a = 600*MPa* and static compression, σ_m = -1200*MPa*, N = 9 x 10^6. In this case, the crack-growth rate *da/dN*, was increased with an increase in crack length. Mode I crack branching was intermittently occurring at shear-mode crack tip. Lengths of the mode I crack were increased with the total length of shear-mode crack 2*a*, and finally the fracture was dominated by mode I. In order to suppress the mode I cracking and to determine threshold condition for shear-mode crack growth, Matsunaga gradually decreases the cyclic shear stress amplitude by 10 to 40*MPa* with every increment in crack length 2*a* of 10 to 30μm. By doing so, little mode I crack branching, if any, was observed [8].

The crack morphology observed in [8] is similar to that occurring in rolling contact fatigue. This is because the loading (cyclic shear and static compression) is similar to that beneath the contact surface as clarified in previous section. Hence, it can be agreed that Matsunaga successfully reproduced the mechanism involved in shear mode crack propagation and threshold in rolling contact condition. Clarifying the observed crack behaviour in his work is necessary in order to understand the mechanism involved in rolling contact fatigue of bearings, rail and similar important engineering components subjected to similar loading condition.

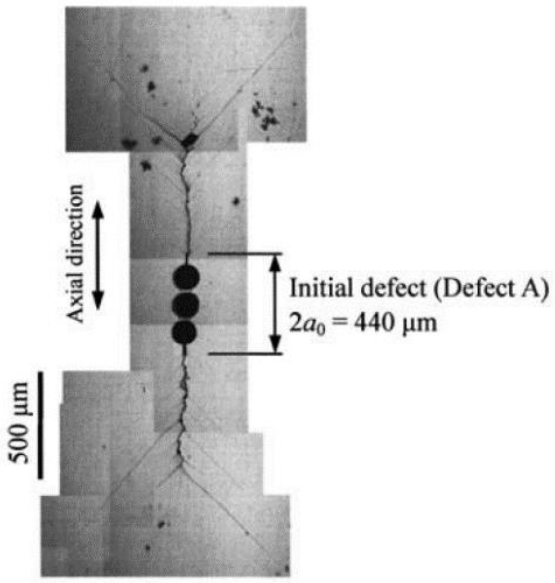

Figure 19 Crack-growth in axial direction and mode I crack branching [8]

1.2 Scope of research and limitations

The aim of this work is to provide improved physical understanding of branch crack mechanics. Starting point of this study is the experimental finding shown by Matsunaga [8] focusing on the influence of compressive mean stress and the interaction of mode I and II cracks i.e. branched cracks. The key research questions based on the previous research in field are:

1. Why does a growing mode I branch crack stop propagating even though the loading condition remain unchanged?
2. When the mode I branch crack can be ignored when estimating the mode II branch crack?
3. What is the nature of the interaction between the mode I crack and the shear mode (mode II and III) crack under compressive mean stress?

In order to provide answer to the aforementioned questions, the thesis consisted of experiment and numerical works as following:

1. Experimental work to determine the effect of stress ratio $\left(R \le -1\right)$ on $\Delta K_{I,th}$ of SAE52100 bearing steel.

2. Determination of the Stress Intensity Factor K_I and K_{II} of branched cracks by Finite Element Method.

Results of this work will provide further insight towards the understanding of the mechanism involved in flaking formation during rolling contact fatigue and its prevention. However, it should be noticed that the present study is focused on the understanding of mechanics, not accurate modelling of crack growth. Thus, the aim is not to provide quantitative answers to the research questions but rather a qualitative one. Consequently, the mechanism involved in the branching of a Mode II crack is not discussed in this work.

2 EFFECT OF NEGATIVE STRESS RATIO ON CRACK GROWTH THRESHOLD

2.1 Objective of experiments

It is known that fatigue cracks grow by Mode I or shear-mode (Mode II and Mode III) beneath the rolling contact surface under a complicated tri-axial stress state. To evaluate the rolling contact fatigue strength as a crack problem on the basis of fracture technology, it is important to reveal the crack growth behaviour of these cracks under compressive mean stress. Previous work [9, 10] on similar high strength steel have concentrated on positive stress ratio or tensile mean stress and stress ratio, *R* not less than -1.

In this study, to elucidate the effect of compressive mean stress on the mode I small crack growth, tension-compression fatigue tests were carried out under various stress ratios. As a result, non-propagating cracks, which are hardly observed at stress ratio *R* of -1 in high strength steel, were observed at the low stress ratio *R* of -10.

2.2 Material and Specimens

Fatigue tests were carried out using on bearing steel, SAE52100, whose chemical composition is shown in Table 1. The specimen is oil quenched for one hour at 840 °C and quenched for two hours at 240 °C. The Vickers hardness was 703 (1 kgf, 30 sec, and 40 points average). Shapes and dimensions of specimen are shown in Figure 20.The specimen's surface was polished with an emery paper and then it was buffed with an alumna paste.

Artificial defects shown in Figure 21 were introduced to the centre of the test section by electrical discharge method (EDM). The size of the artificial defect, selected in this work, falls on the threshold of the transition size from small crack behaviour to large crack behaviour for this material, as shown in Figure 22, hence it can be regarded as a small crack. In Figure 22, obtained from a sister research work going in the same laboratory, artificial defects of three different sizes were tested at R = -1 for the same material (SAE52100, HV =703) as this work and the threshold condition for crack propagation for each sizes was obtained. The dotted straight line is the plot of the fatigue limit prediction equation proposed by Murakami and Endo for small cracks, the equation is shown in the figure as well. The SN curves, for the three artificial defect sizes, from of the tests are shown in Figure 23.

Table 1 Chemical composition of bearing steel, SAE52100.

C	Si	Mn	Cr	Ti	O
1.00	0.26	0.36	1.44	0.002	0.0006

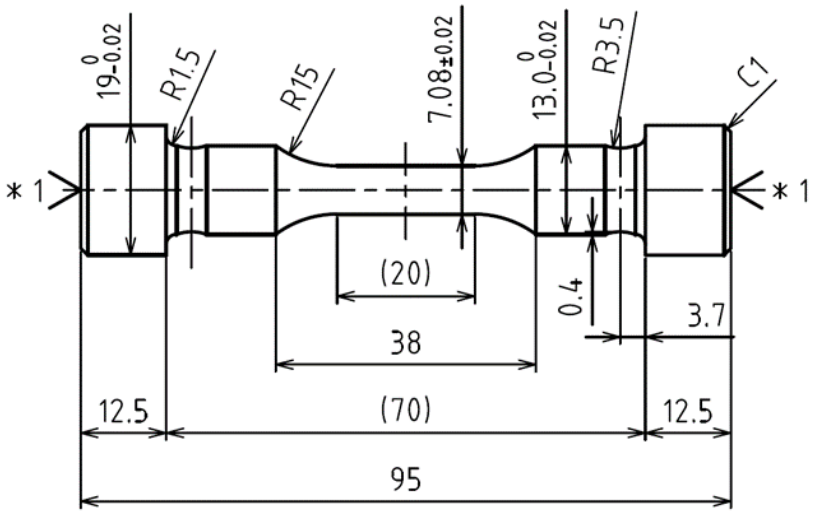

Figure 20 Shape and dimensions of specimen in mm.

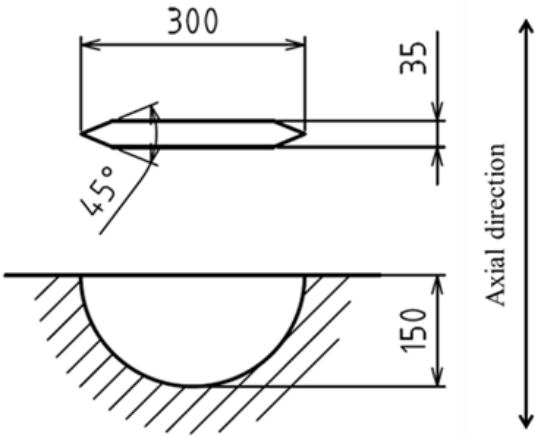

$2a = 300\mu m, \sqrt{area} = 188\mu m$

Figure 21 Shape and dimensions of artificial defect in μm.

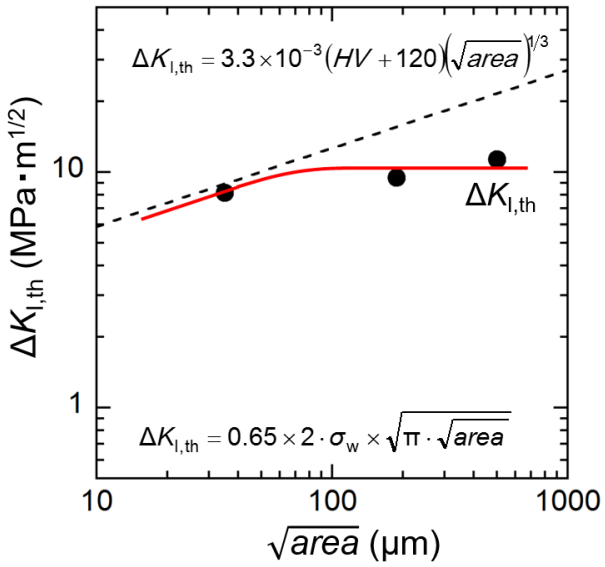

Figure 22 Crack size dependence of $\Delta K_{I,th}$ of SAE52100

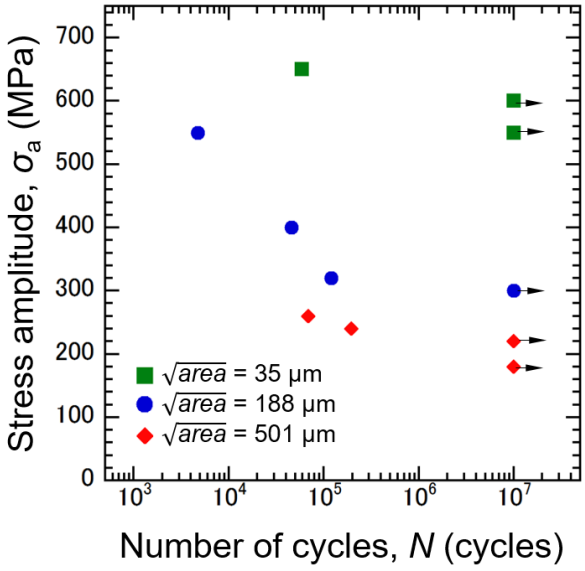

Figure 23 Stress amplitude – Life curve for three artificial defect sizes.

2.3 Fatigue Test

Tension-compression fatigue tests was carried out using a servo-hydraulic fatigue testing machine with a testing frequency of 20Hz for all *R* values. Before beginning each test, strain gauges were attached to the surface of the specimen and the strain readings were monitored

on a screen during the installation of the specimens to the test machine, aim of this exercise is to prevent any bending effect due to misalignment. The tests were periodically halted for microscopic observation of initiation and crack-growth using the replica method. Test was stopped if the specimen did not fail after 10^8 cycles. Fatigue limit is defined as the threshold stress level for non-propagation of cracks however in very hard steel such as the one investigated, non-propagating crack is hardly observed [5]. However, it is also known that for such hard material the difference between threshold stress level for crack initiation is very close to that of crack propagation, hence in this work we shall define fatigue limit at the threshold stress level for initiation or propagation of crack. At each stress ratio, the first test stress level is selected with the intention that the specimen will fail, then the next test is performed with a reduced stress level. The reduction depends on the test result of the previous test.

2.4 Experimental Results

The maximum applied stresses and their test result for each *R* value is summarised in Figure 24. Figure 24 also shows the variation of the magnitude and variation of the stress amplitude at each *R* value. Figure 26 shows the $K_{\mathrm{Imax,th}}$ and $\Delta K_{\mathrm{I,th}}$ at the fatigue limit for the stress ratios investigated. It can be seen that the trend of Figure 24 and 26 follows that the results obtained by Kondo et.al as discussion in previous chapter. The obtained test results deviate very much from widely used mean stress correction model including the classical models such as modified Goodman equation and those based on crack closure models. The reason for this can be seen in Figure 14 (a and b). It can be concluded that no model exist which can predict the threshold stress intensity factor or fatigue limit of small crack under compressive mean stress with reasonable accuracy.

At *R* = -1 -3 and -5, Non-Propagating Cracks (NPC) were not observed at the fatigue limits by replica and microscopic observation method used in this work, however, at *R* = -10, clear non-propagating cracks were observed at the fatigue limits. It may be that NPC is indeed presence but is too short to be observed by the technique used for observation or perhaps smaller stress range step is required in other to observed NPC at other stress ratios.

In an attempt to clarify why NPC was not observed/clearly visible at other stress ratio other than at *R* = -10, new set specimens for the same material was prepared with smaller artificial defect but same geometry (root area = 125µm, $2a_{\mathrm{int}}$ = 300µm). This specimens was tested at

stress ratio R = -5 and -10 only. NPC was observed for both R-value. Figure 25 shows the NPC observed for the two artificial defect sizes at R = -5 and -10. Experimental working is ongoing to clarify the appearance or non-appearance of NPC at fatigue limit of this material under compressive mean stress.

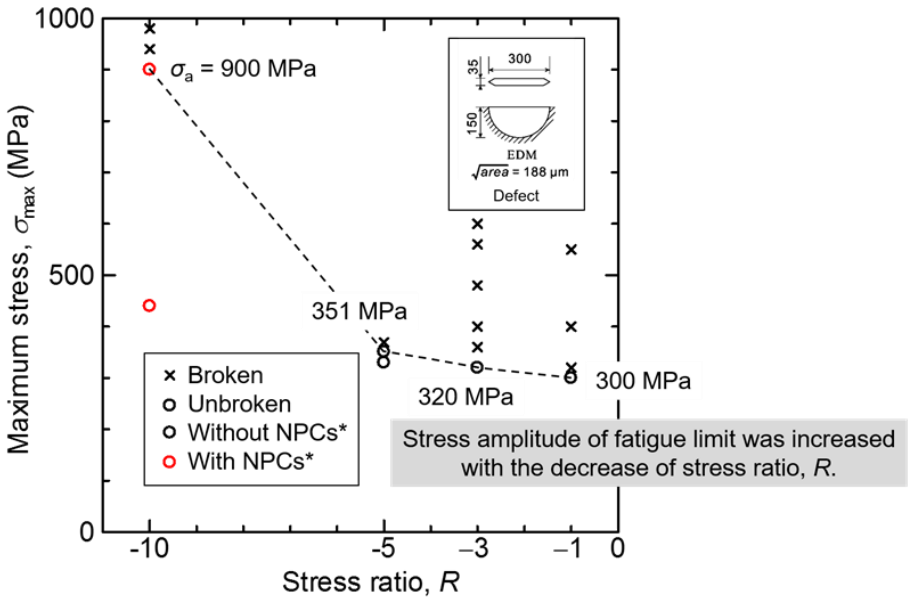

Figure 24 Relationship between Maximum stress and stress ratio R

Stress intensity factor, $K_{I,th}$ is calculated using Murakami's Equation [5].

$$K_{I,th} = 0.65 \times \sigma_{th} \times \sqrt{\pi \cdot \sqrt{area}} \quad (15)$$

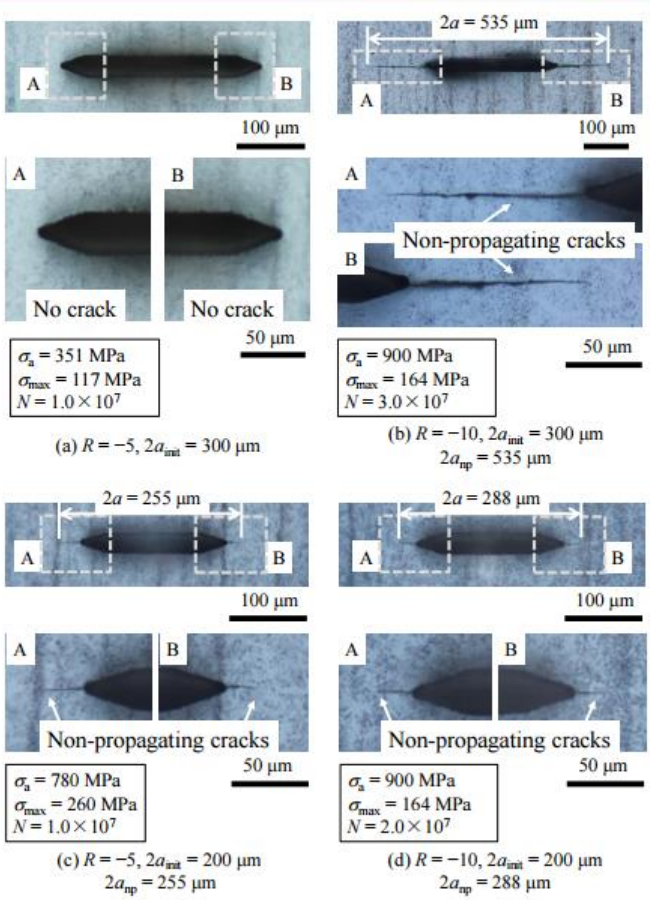

Figure 25 Non-propagating cracks observed after fatigue tests.

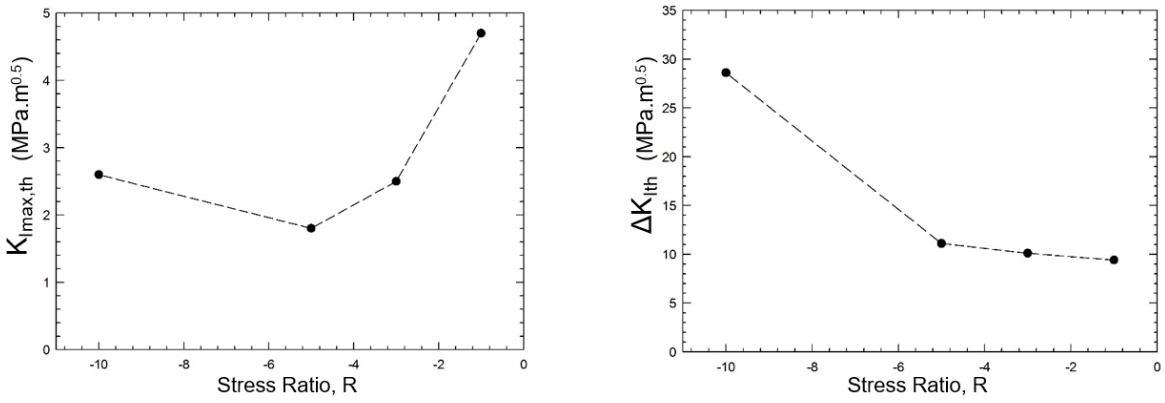

Figure 26 $K_{\mathrm{I}max,th}$ and $\Delta K_{I,th}$ as a function of stress ratio, *R*.

Two important conclusions can be drawn from the experimental results:

1. $\Delta K_{I,th}$ increases with increase in compressive mean stress or as stress ratio, R decreases.
2. NPC which are hardly observed in high strength steel at fatigue limit, were observed at stress ratio of -5 and -10.

3 STRESS INTENSITY FACTOR OF BRANCHED CRACK

3.1 Objective of numerical analysis

Determination of the SIF of a crack is one of the most important step in using LEFM for static and fatigue failure prevention. The evaluation of stress intensity factor (SIF) in 2D and 3D geometries by means of the Finite Element Method (FEM) is a technique widely used for non-standard crack configurations, such as kink crack, curved crack and branched crack, whose solution are not available in handbooks [15]. Other numerical methods such as Body Force Method (BFM), Distributed Dislocation Method (DDM) had also been used in the past. Several researchers have studied the SIF of branched/kinked crack [16, 17]. The crack type already investigated and the loading conditions are shown in Table 1. However in this work, branch crack morphology and loading condition shown in Figure 27, which is similar to that observed under rolling contact loading [1, 2, 3, 6 and 8], is studied. To the best of the knowledge of the author, such branch crack morphology and loading has not been investigated before, despite its practical importance.

The numerical analysis of this study is done by FEM. In FEM, the structure or part is discretized as elements. Each element has stiffness and they are connected to each other by nodes. When part is loaded, its deformation, displacements and stresses can be calculated by solving the systems of equations. In the estimation of the SIF by FEM, once the numerical solution has been obtained for a particular finite element representation, crack tip stress intensity factors can be estimated by using established crack tip relations [14]. There are many possible methods which can be used for example, the displacement method, the stress method and the j-integral method. The stress method will be used in this work due to its relative simplicity and ease of interpretation [14]. The stress method involves a correlation of the finite element nodal point stresses with the well-known crack tip stress distribution equation [14].

Table 1 Previous work on SIF of branched/kinked crack

Researcher	Crack Problem Solved	Method Used
Kitagawa [17]	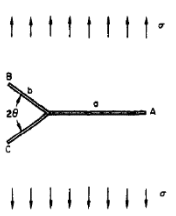	Conformal Mapping Method
Isida [16]	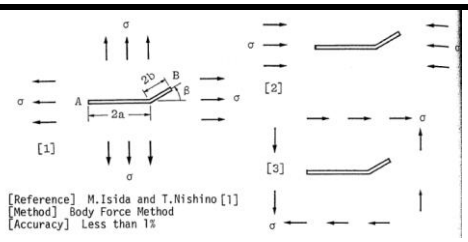	Body Force Method
Kitagawa [17]	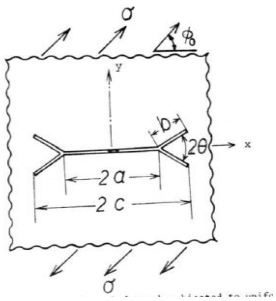	Conformal Mapping Method

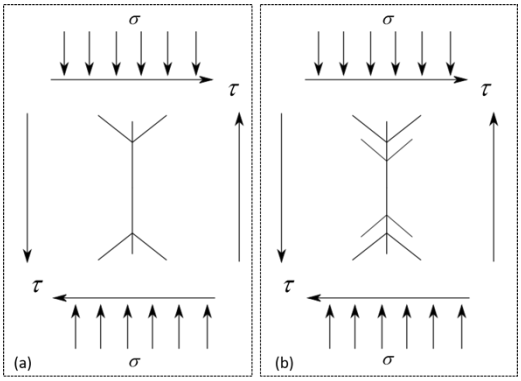

Figure 27 Branch cracks to be studied in this work. (Branching angle is 45_degrees. This angle is based on the experiment observation).

Equation (13) is the key to the Stress Method first proposed by Chan et al. [14] on how to estimate the Stress Intensity Factor of an arbitrarily shaped crack using FEM. This method does not require the use of any singular element at the crack tip. The method is adopted in this work and detailed description of the method can be found in [14].

For mixed mode situation in plane problem, the stress intensity factor K_I and K_{II} can be obtained by extrapolating the curve of K_I^* and K_{II}^* respectively to r = 0.

Where,

$$K_I^* = (2\pi r)^{1/2}\sigma_{yy}$$

$$K_{II}^* = (2\pi r)^{1/2}\tau_{xy} \qquad (16)$$

In equation 16, the crack axis is taken as x-axis in the x-y plane (see Figure 25). K_I^* and K_{II}^* are obtained from 10 data points from the crack-tip.

3.2 Modelling Technique and Software

NX 9.0 is used for solid body modeling and NX Nastran 10.0 Advanced Simulation is used for preprocessing and solving. In all simulation, a thin square plate of side length *L* (see Figure 28) is used. The value of L is chosen such that $L \geq 10C$, where C is crack length varying from 1mm to 3.5mm. By doing so, an infinite plate is simulated for all crack lengths. Similar requirement was set for two-branch crack morphology. The plate thickness is 0.05mm in all simulation, this value is also the mesh size used in all simulations, and hence there were just one layer of element. The mesh size used was selected after numerous iteration with smaller and bigger size for simulations with known solution. It was concluded that the adopted mesh size of 0.05mm will be adequate and accurate enough for this work without.

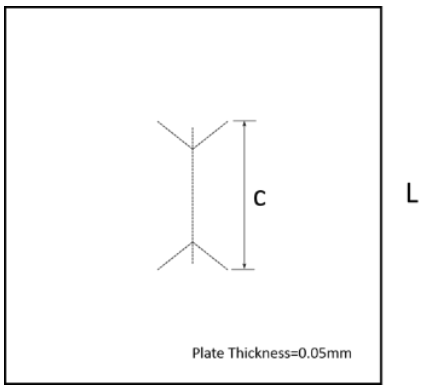

Figure 28 Plate geometry used in the simulations. Branching angle is 45º

The most important step in the geometry preparation is the modeling of the crack in the plate. The "cut and sew" technique adopted in this work will be explained using a V-shaped crack as an example.

Step 1 - Make 3D model of the plate without any crack

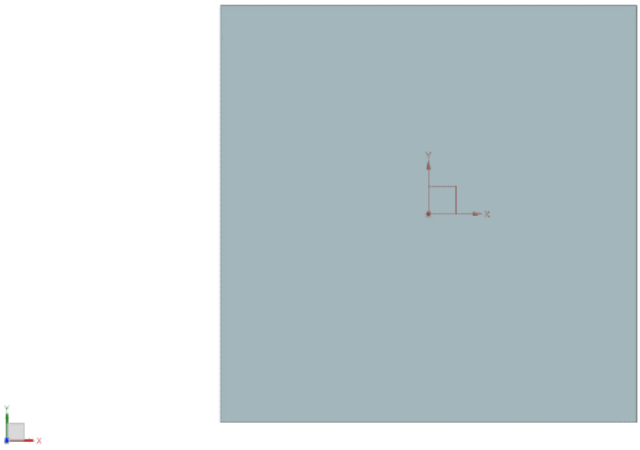

Figure 29 Plate used in the simulations (without crack).

Step 2 - Split the body into parts in such a way keeping in mind the desired crack shape.

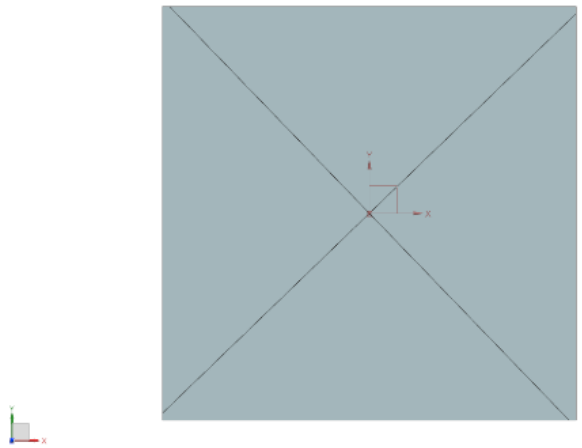

Figure 30 Plate use in the simulation (divided into parts)

Step 3 – Divide the faces/surfaces of the parts in such a way that regions where there is no crack can be rejoined.

Step 4 – Join regions where no crack is intended using surface-to-surface glue command (this command will merge the opposite nodes during solution). Join regions that the crack is intended with surface-to-surface contact command (this command will prevent the pair of surfaces selected from overlapping and also account for frictional force). Coefficient of friction can be specified as well.

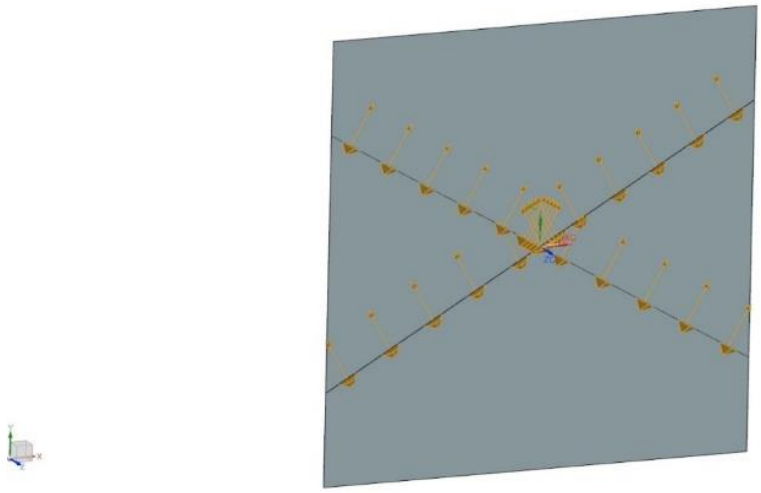

Figure 31 Sewed plate with surface-to-surface conditions

In principle, this technique can be used to modelled cracks of any morphology, also three-dimensional cracks can be modelled in this way. First step in the meshing stage is to specify the so called *mesh mating condition* at regions that a surface-to-surface condition is specified (see step-4 of previous section). This does not only lead to an improvement in the analysis result but also it help to avoid convergence problem.

20-node-chexa 3D element was used in all simulations. Mesh size was 0.05mm (same as plate thickness). Figure 32 show meshes in the case of a V-shape crack. A local coordinate system (x-axis is taken along the particular crack segment axis) is created at this stage which will be during post-processing to read the nodal stresses needed to compute the stress intensity factor at the crack-tip.

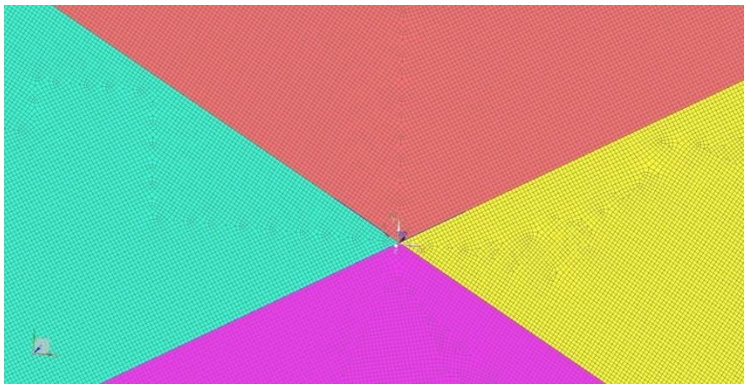

Figure 32 Meshed plate containing V-shaped crack

The loadings are applied as distributed surfaces forces which are calculated as the product of the desired stress level and surface area as shown in Figure 33.

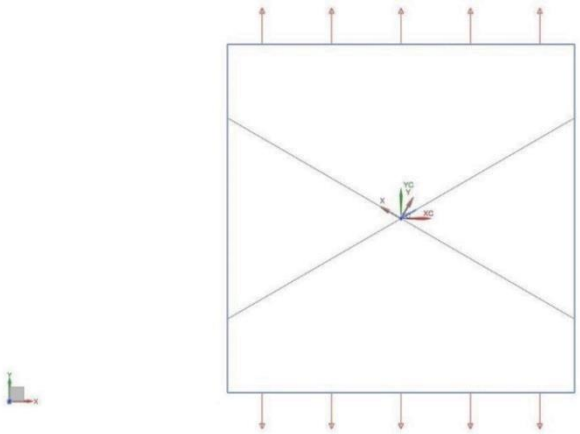

Figure 33 Loading on the plate surfaces for simulation

NX Nastran 10 Advanced Simulation has a special function called “inertia relief”, by activating this function, there is no need to specify a displacement constraint. This feature is utilized in all simulations. The mathematical principle involved in this function is available in NX Nastran manuals.

3.3 Computation method for Stress Intensity Factor

The stresses at few nodal points from the crack-tip whose SIF’s is to be computed is extracted from the analysis result using the local coordinate system of the crack segment in question as shown in Figure 34. The K_I* and K_{II}* for the points can be computed using equation 16. From this curves, the K_I and K_{II} can be obtained by extrapolation [14].

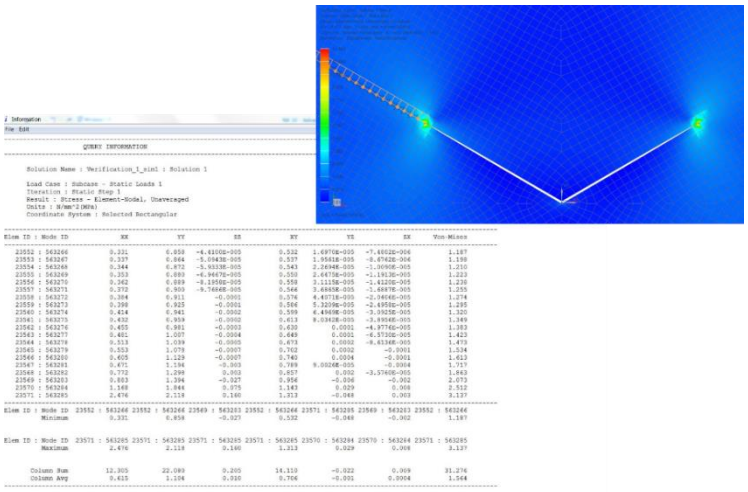

Figure 34 Extraction of nodal stress point near crack-tip

3.4 Validation of numerical simulations

In order to obtain some confidence on the accuracy of the modelling techniques discussed above, the author applied the procedures to two verifications models. Verification Model 1 is a V-Shaped crack under uniaxial tension applied at infinity as shown in Figure 35. The reference solution is the work of TerMaath [19]. The loading conditions and crack geometry obtained from [19] are given below: $\sigma_y^\infty = 1MPa, \sigma_x^\infty = 0$ and $\tau_{xy}^\infty = 0$. Unit crack segment lengths $(a_1 = a_2 = 1mm)$ and $w = 120^o$. Table 2 lists results from this work and from [19]. It can be seen that the computed values from both methods are very similar.

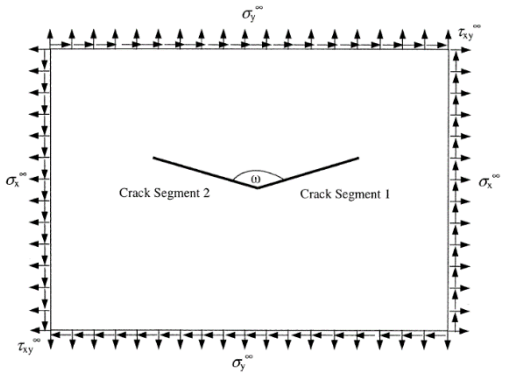

Figure 35 V-Shaped crack in an infinite plate [19]

Table 2 SIF for a V-shaped crack under uniaxial tension loading

	K_I $\left[MPa\sqrt{mm}\right]$	K_{II} $\left[MPa\sqrt{mm}\right]$
Ref [19]	1.255	0.846
This work	1.267	0.838

Verification Model 2 is a bent crack under biaxial loading, compression and shear loading applied at infinity as shown in Figure 36. The reference solution is the work of Isida [16].

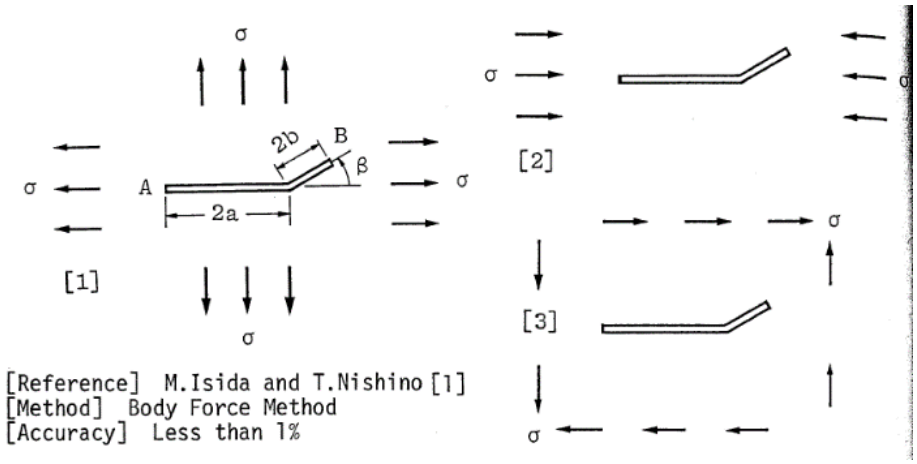

Figure 36 Bent crack in an infinite plate [19]

Table 3 lists results from this work and from [16]. It can be seen that the results from this work are very similar to those reported in the references except verification 2c, the reason

for this could be that in this work the crack surfaces are prevented from overlapping by specifying coefficient of friction as 0.001, however in [16] there was no mention of such boundary condition.

Table 3 SIF for a bent crack under biaxial, compression and shear loading

(a) Biaxial loading, $\sigma = 1MPa$, $a = 1.0mm$, $b = 0.1mm$ and $\beta = 45^o$.

	K_I $\left[MPa\sqrt{mm}\right]$	K_{II} $\left[MPa\sqrt{mm}\right]$
Ref [16]	1.513	0.557
This work	1.535	0.563

(b) Compression loading, $\sigma = 1MPa$, $a = 1.0mm$, $b = 0.1mm$ and $\beta = 45^o$.

	K_I $\left[MPa\sqrt{mm}\right]$	K_{II} $\left[MPa\sqrt{mm}\right]$
Ref [16]	-0.352	0.370
This work	-0.352	0.392

(c) Shear Loading, $\tau = 1MPa$, $a = 1.0mm$, $b = 0.1mm$ and $\beta = 45^o$.

	K_I $\left[MPa\sqrt{mm}\right]$	K_{II} $\left[MPa\sqrt{mm}\right]$
Ref [16]	-1.789	0.903
This work	-1.465	0.791

3.5 Results for branch cracks configuration

Two crack morphologies are studied in this work. Figure 37 and 38 shows the geometry of what will be refer to as *one-branch crack* and Figure 39 shows the geometry of *two-branch crack.* In the *two-branch crack*, the first branch length is fixed as 1mm and the distance between the two branches is fixed as 0.25mm.

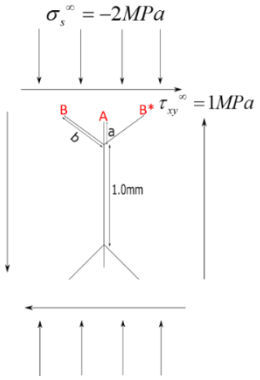

Figure 37 One-branch crack, constant stress and varying crack lengths

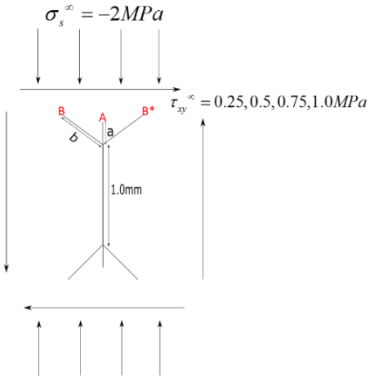

Figure 38 *One-branch crack*, varying shear stress and crack length

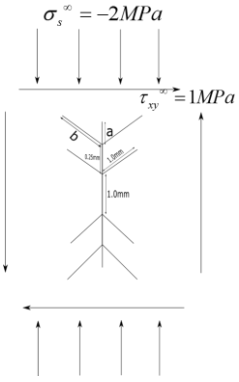

Figure 39 *Two-branch crack*, constant stresses and varying crack lengths

Two kind of analysis were performed on *one-branch crack*. In the first analysis, the stresses were kept constant while the Mode I crack length *b*, and Mode II crack length *a*, were varied. In the second analysis both the crack sizes, *a* and *b* and shear stress were varied as shown in Figure 38. For the *two-branch crack*, only the former kind of analysis was performed.

The following data was obtained by the procedures discussed in previous sections.

a) Mode II Stress Intensity Factor , K_{II}^{A} at point *A*
b) Maximum Mode I Stress Intensity Factor , K_{I}^{B} at point *B*
c) Minimum Mode I Stress Intensity Factor , $K_{I}^{B^*}$ at point *B**

From result (a), (b) and (c) the following useful parameters can be calculated

a) Mode II Stress Intensity Range at *A*, $\Delta K_{II}^{A} = 2 \times K_{II}^{A}$.
b) Mode I Stress Intensity Range at *B* and *B**, $\Delta K_{I}^{B} = \Delta K_{I}^{B^*} = K_{I}^{B} - K_{I}^{B^*}$.
c) Stress Ratio at *B* and *B**, $R = \frac{K_{I}^{B^*}}{K_{I}^{B}}$.

The variation of ΔK_{II}^{A}, ΔK_{I}^{B} and *R* for all combinations of crack lengths *a*, *b* and stress level studied in this work will be used to provide answer to the research questions in chapter 1.

In the next paragraphs, questions will be put forward and followed by the analysis result (as Figure or Table. Observation and comments on these figures will be given in the discussion section in conjunction with the experiment results), the author thinks that presenting the results in this way, will help the reader understand them better and also to avoid repetition. That been said, a keen reader may already observed some interesting points.

I. How does ΔK_I^B and R change for a constant stress levels $\left(\sigma_\infty = -2MPa, \tau_\infty = 1MPa\right)$, constant Mode I crack length but varying Mode II crack length? A careful reader can observed that the curves of ΔK_I^B and R for b = 0.25, 0.50 and 0.75 shows similar tendency. The turning point of the curves (which appears to be approximately at same shear mode crack length) is another important observations which will be discussed further in the result analysis section.

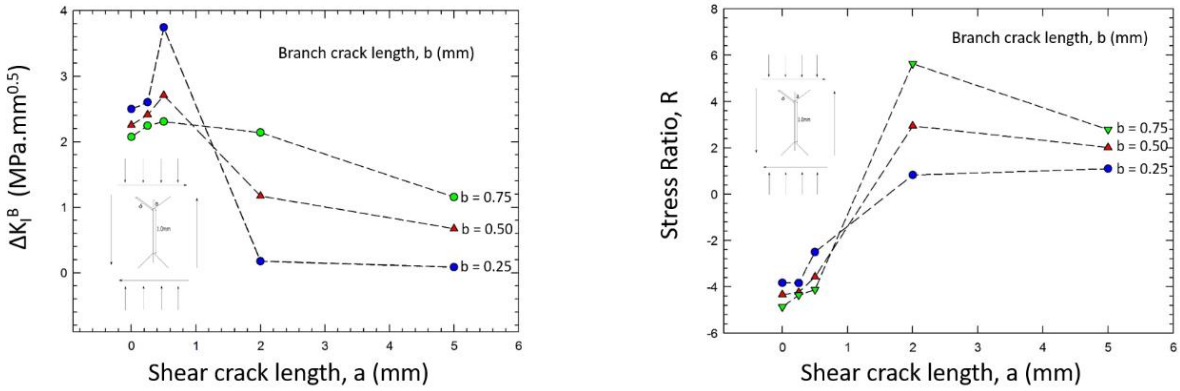

Figure 40 Variation of ΔK_I^B and R for constant stresses $(\sigma_\infty = -2MPa, \tau_\infty = 1MPa)$ and varying *a* and *b*.

II. How does ΔK_I^B changes for a constant Mode I crack length, constant Mode II crack length and compressive stress $\sigma_\infty = -2\text{MPa}$ but varying shear stress? In this analysis only one shear mode crack length (a = 0.5 mm) was simulated and two mode I crack lengths (b = 0.25 and 0.5mm). Th variation of ΔK_I^B curves for both mode I cracks is similar. Further observations will be discussed in the result analysis section.

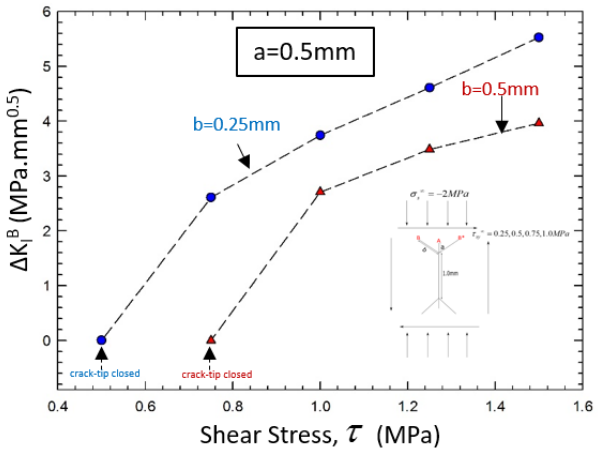

Figure 41 Variation of ΔK_I^B for constant σ_∞ , a and varying τ_∞ and b.

III. How does ΔK_{II}^A changes for a constant stress levels $\sigma_\infty = -2\text{MPa}, \tau_\infty = 1\text{MPa}$, constant Mode II crack length but varying Mode I crack length? Approximate value is calculated with equation below (ignoring the presence of the branch cracks).

$$\approx \Delta K_{II}^A = \tau_\infty \sqrt{\pi(0.5+a)}, \qquad \approx \Delta K_{II}^A = \tau_\infty \sqrt{\pi(0.75+a)}$$

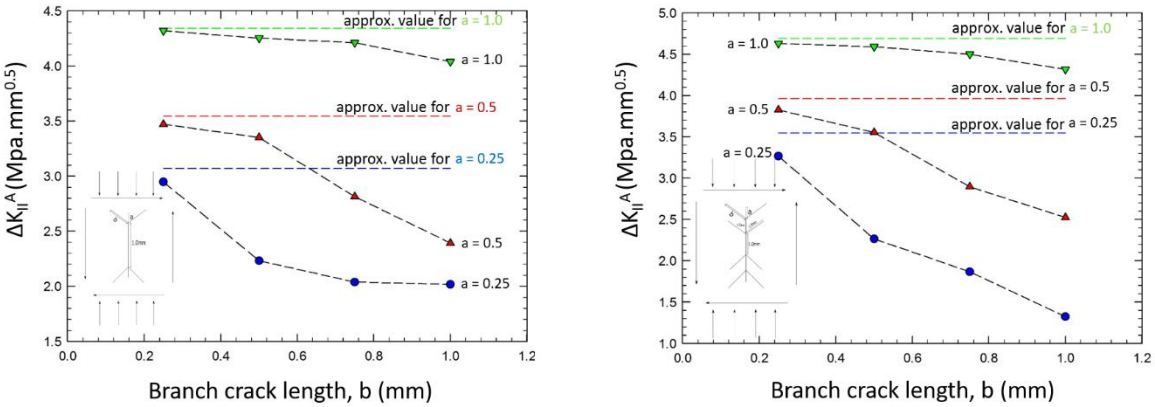

Figure 42 Variation of ΔK_{II}^A for constant stresses $(\sigma_\infty = -2MPa, \tau_\infty = 1MPa)$ and varying a and b.

4 RESULTS ANALYSIS

In order to provide answer to the research objectives of this work, the experimental result of chapter 2 will be combined with the FEM result and rational argument will be put forward. The arguments proposed does not consider the small crack effect on ΔK_{th}, that is , it is assumed that the mode I and II crack are at such length that ΔK_{th} does not depend on crack size.

On why a growing mode I branch crack stop propagating even though the loading condition $\pm\tau_{\mathrm{a}} = 600\mathrm{MPa}, \sigma_{\mathrm{m}} = -1200\mathrm{MPa}$ remain unchanged, reference should be made to Figure 40 and 26. The following observation can made from Figure 40. The applied stresses were $\sigma_{\infty} = -2\mathrm{MPa}, \tau_{\infty} = 1\mathrm{MPa}$.

1. When the mode II crack length *a*, is less than 1mm, an increase in mode I crack length b, leads to a decrease in ΔK_I^B and the stress ratio *R*, becomes smaller.
2. When the mode II crack length *a*, is greater than 1mm, an increase in mode I crack length *b*, leads to an increase in ΔK_I^B and the stress ratio *R*, increases and even reached non-negative value at $\mathrm{a} \geq 2\mathrm{mm}$.
3. $\Delta K_{I,th}$ increases as stress ratio, *R* becomes smaller.

The three observations above clearly show that the non-propagating behaviour of the mode I crack, even though the applied stress level was maintained constant, is due to the influence of the mode II crack. When the mode II crack length a, is relatively short, as the mode I crack grows, resistance to propagation $\Delta K_{I,th}$ increases due to more negative stress ratio while at the same time ΔK_I^B decreases. If the situation $\Delta K_{I,th} \geq \Delta K_I$ occurs, the mode I crack will stop propagation. The opposite is the case when the mode II crack is relatively longer. It will be shown later that the mode II crack length when this transition occurs depends on the ratio, $\chi = -\sigma_{\mathrm{static}} / \tau_{\mathrm{cyclic}}$ of the applied static compression and cyclic shear stress. This not only explains why a growing mode I crack can stop propagation but also why the length of the non-propagating mode I crack varies as mode II crack grows and also why mode I crack may not stop to propagate i.e. leads to failure. The mode I and II crack growth rates of the material

will also play a controlling role in this phenomenon, likewise any other factors that influence the crack growth rate such as environment and friction.

On why reducing the applied cyclic shear stress while maintain the magnitude of the static compression (that is, increasing the absolute value of the ratio, $\chi = -\sigma_{\text{static}} / \tau_{\text{cyclic}}$) results to little or no mode I crack branching, reference should be made to Figure 41. From which following observations can be made from Figure 41. The applied stresses are $\sigma_\infty = -2\text{MPa}, \tau_\infty = 1.5, 1.25, 1.0, 0.75$ and 0.5MPa .

1. As the magnitude of applied shear stress τ reduces, the ΔK_I^B reduces.
2. For a fixed value of mode I and mode II crack length, there is a value of shear stress τ such that ΔK_I^B of the mode I crack becomes zero. In other words, there is a value of χ^*, such that ΔK_I^B of mode I is zero (the crack tip was totally closed).
3. The value of χ^* depends on the mode I crack length, the smaller the value of the mode I crack, the higher the value of χ^*.

The three observations above clarify the role of the static compressive stress in suppressing the mode I crack. If a mode I crack initiate and is growing under a given cyclic shear stress and static compressive stress, its propagation can be suppresses by increasing the value of χ to χ^*. This can be achieve either by increasing the value of the static compressive stress (but staying below the material yield strength) or by decreasing the value of the cyclic shear stress. Matsunaga [8] decreased the cyclic shear stress to suppress the mode I crack.

On the question, can the mode I branch crack be ignored when estimating the ΔK_{II}^A at the tip of the non-propagating shear mode crack, reference should be made to Figure 42. From which following was made. The applied stresses was $\sigma_\infty = -2\text{MPa}, \tau_\infty = 1\text{MPa}$.

1. As mode I crack length increases, ΔK_{II}^A for a fixed mode II crack decreases. The decreasing effect is more pronounced in two-branch configuration than one-branch.
2. ΔK_{II}^A for all mode II crack length is very close to its approximate value (estimated by ignoring the presence of the mode I crack) when the mode I crack length is relatively short.

Based on these two observations, it can be agreed that if the mode I crack is short, for example, 0.25mm the ΔK_{II}^{A} can be estimated ignoring the mode I cracks. However, when the mode I crack is not short, ΔK_{II}^{A} could be smaller than its approximate value by as much as 65% in one-branch configuration and 37% in two-branch configuration.

Yet another way to interpret Figure 42 is as follows; Imagine that mode I and mode II crack are growing but mode I crack is growing much faster. As a result of this growth rate, Figure 40 predicts that if ΔK_{II}^{A} reduces (although mode II crack length is increasing as well but at a slower rate) below $\Delta K_{II,th}$, it will become non-propagating.

It can be seen that there is a competition or interaction between mode I crack and mode II crack, the nature of this completion is controlled not only by the applied stresses but also the crack growth rates of the material.

5 CONCLUSION

In this study, mechanism of flaking formation in rolling element, e.g. bearings and rails were investigated. This work is continuation of work of [8] on bearing steel, where authors were able to reproduce the stress state beneath a rolling element laid the foundation for this study. The crack behaviour observed in his work is similar to that leading to flaking in bearings, hence if we can understand this behaviour, it will be a significant achievement towards understand and preventing flaking, not only in bearings but also in other engineering components under rolling contact loading. Two related works were carried out for this work. Experimental work to investigate the effect of negative stress ratio, R or compressive mean stress on $\Delta K_{I,th}$ of SAE52100. The other work was the determination of the ΔK_I and ΔK_{II} of complicated branch crack under cyclic shear stress and static compressive stress by finite element method. The results of these two works were used to explain the observed crack behaviour in [8].

In the experimental work, $\Delta K_{I,th}$ for R = -1,-3,-5 and -10 were obtained. The experimental results clearly show that $\Delta K_{I,th}$ increases as R values decreases. Non-propagating crack, about $535\mu m$ long, which was hardly observed for hard steel was observed at R = -10. The mechanism leading to its appearance at this stress ratio is still unclear.

Finite element method was used to determine the ΔK_I and ΔK_{II} of two different branch configurations, in some cases the applied stresses were kept constant while the mode I and mode II crack lengths were varied. In other cases, both the stresses and the crack lengths were varied. A very systematic investigation of the effect of lengths of mode I and mode II cracks were carried out. The results of this work made clear the nature of the competition between the mode I crack and the mode II crack.

The experimental and simulation results showed that there is a competitive behaviour between the Mode I and Mode II crack growth. The role of the compressive mean stress is to suppress the Mode I crack propagation. The magnitude of the compressive mean stress required to suppress Mode I crack growth depends on the Mode II crack length and applied

cyclic shear stress. It was also observed that mode I crack lengths, if long enough, may reduce the K_{II} of the Mode II crack even by 63%.

The observation of non-propagating cracks for high compressive mean stress is one of novel finding of this study. However, the physical reason for this is not yet know. This is left future work. Furthermore, the numerical investigations can be extended to study more detail the influence of crack surface friction on crack growth mechanics.

6 FUTURE WORK

Although all the research questions was successfully answered, some questions still remain. The role of coefficient of friction on the computed ΔK_{II} is still unclear. In this work, a fixed value of 0.6 was used and additional analysis are recommended. Furthermore, FEM adopted in this work was computationally expensive. Very fine mesh had to be used in order to obtain accurate result. A numerical method such as Body Force Method (BFM), Distributed Dislocation Method (DDM) should be utilised in future as well. Future work should be focused on also the reason for the appearance of NPC, $535\mu m$ long, at *R*=-10 whereas at other strass ratio studied in this work there was no NPC, should be clarified.

REFERENCES

[1] Sadeghi, F., Jalalahmadi, B., Slack, T., and Raje, N., 2009, "A Review of Rolling Contact Fatigue," ASME J. Tribol., 131(1), p. 041403.

[2] Ebert F J. Fundamentals of design and technology of rolling element bearings. Chinese Journal of Aeronautics 2010; 23:123-136.

[3] Lou, B., Han, L., Z., Liu, S., and Shen, F., 1990, "The Rolling Contact Fatigue Behaviors in Carburized and Hardened Steel," Fatigue 90: Proceedings of the Fourth international Conference on Fatigue and Fatigue Thresholds, Honolulu, HI, H. Kitagawa and Tanaka, eds., pp. 627-632.

[4] N. M Belayev, loc. cit., page 12. Journal of Applied Mechanics, ASME, 1935

[5] Y. Murakami. Metal Fatigue: Effect of small defects and non-metallic inclusions. - Oxford: Elsevier, 2002.

[6] M. N. Lewis, B. Tomkins, A fracture mechanics interpretation of rolling bearing fatigue, P. I. Mech. Eng. J-J. Eng., 226(2012) 389-485.

[7] D.F. Socie and G.B Marquis, Multiaxial Fatigue (Society of Automotive Engineers, Inc., Warrendale, PA, USA, 2000).

[8] H. Matsunaga, S. Muramoto, N. Shomura, and M. Endo, J. Soc. Mater. Sci., Japan, **58**(9), 773(2009).

[9] Y. Murakami, Y. Uemura, Y. Natsume and S. Miyakawa, "Effect of Mean stress on the Fatigue Strength of High-Strength Steels containing small defects or Nonmetallic Inclusions", Transactions of the Japan Society of Mechanical Engineers, Vol. 56, No 525, pp. 1074-1081(1990).

[10] Y. Kondo, C. Sakae, M. Kubota and T. Kudou, "The effect of material hardness and mean stress on the fatigue limit of steels containing small defects", Fatigue and Fracture of Engineering Structures, Vol. 26, No.8, pp. 675-682(2003).

[11] W. Elber, "Fatigue crack closure under cyclic tension", Engineering Fracture Mechanics, Vol. 2, No.1, pp. 37-45 (1970).

[12] W. Elber, “The significance of Fatigue Crack Closure”, Damage tolerance in aircraft structures, pp. 230-242 (1971).

[13] O. C. Zienkiewicz and Y. K. Cheung, The Finite Element Method in Structural and Continuum Mechanics. McGraw-Hill, New York (1967).

[14] S. K. Chan, I. S. Tuba and W. K. Wilson, “On the Finite Element Methods in Linear Fracture Mechanics” Engineering Fracture Mechanics, Vol. 2, pp, 1-17 (1970).

[15] Murakami, Y., 1987. Stress Intensity Factors Handbook. Pergamon Press, New York.

[16] M. Isida and H. Noguchi, Formulae of Stress Intensity Factors of Branched Cracks in Plane Problems, Trans. Japan Soc. Mech. Engrs., Vol. 49-440 (1983), pp. 469-479.

[17] H. Kitagawa and R. Yuuki, Stress Intensity Factors for Branched Cracks in a Two-Dimensional Stress State, Trans. Japan Soc. Mech. Engrs., Vol. 41-346 (1975). Pp. 1641-1649.

[18] Lawn, B.R. and Shaw, T.R. (1975) Fracture of Brittle Solids, Cambridge University Press, Cambridge.

[19] TerMaath S. A two-dimensional analytical technique for studying fracture in brittle materials containing interacting kinked and branched cracks. Dissertation, Cornell University, 2000.

[20] Anti-Friction Bearing Manufacturers Assoc., Inc., Ball bearing comparison with roller bearing, viewed 2 January 2017, < https://www.britannica.com/technology/bearing-machine-component/images-videos/Rolling-bearing-ball-bearing/4471>.